Supplementary Figures

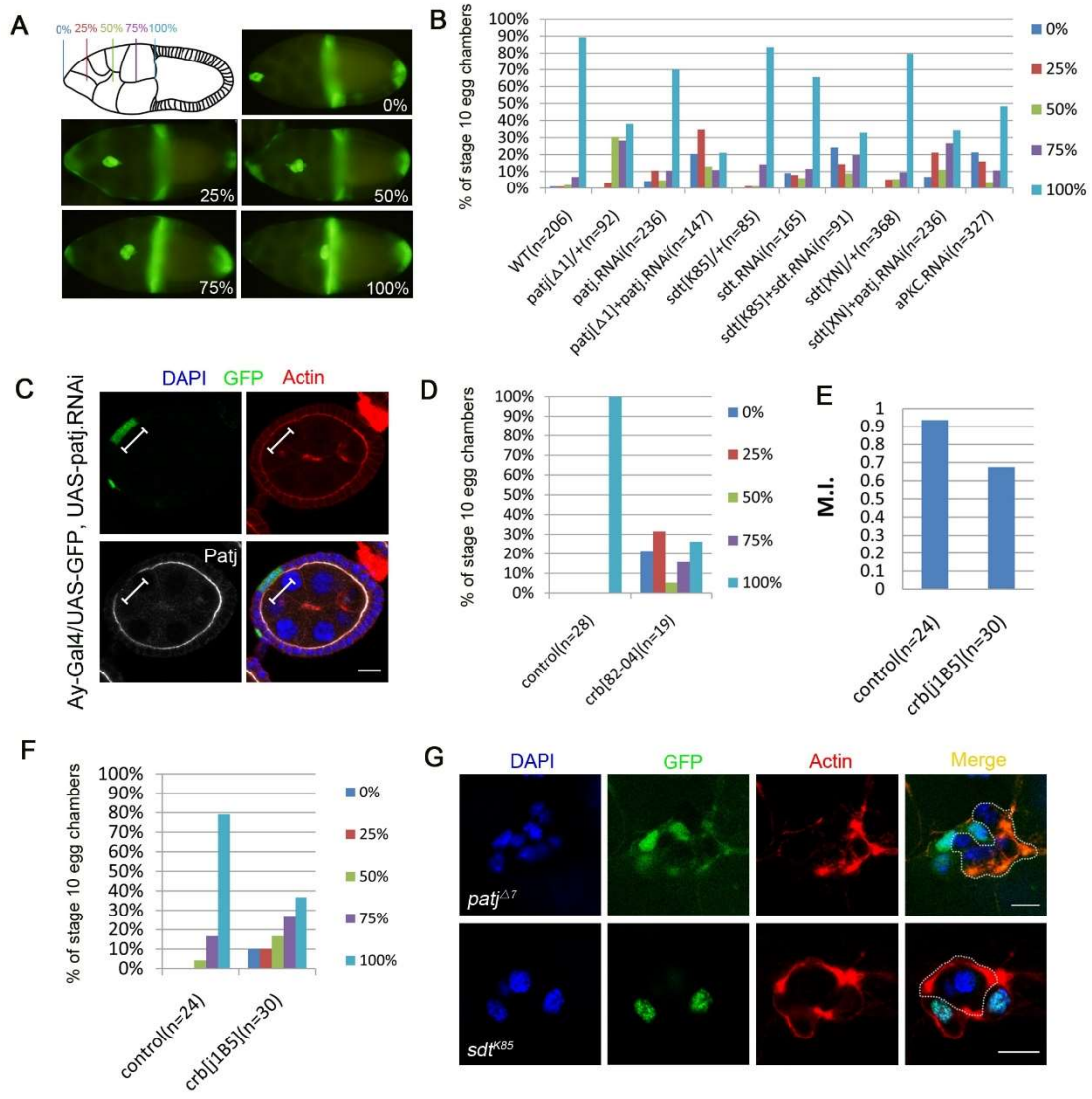

Figure S1. Crb complex components and aPKC are required for border cell migration.

(A) A diagram and fluorescent images showing the extent of border cell migration for stage 10 egg chambers. In wild type, border cells normally have completed posterior migration at stage 10, and it is represented in the "100%" migration category. The categories of 0% (no migration), 25%, 50% and 75% represent different degrees of migration delay. (B, D-F) Quantification of border cell migration. The Y-axis denotes the percentage of stage 10 egg chambers that exhibit each degree of migration, as represented by five color-coded bars for each genotype (B, D, F). (E) Migration index

(MI) of mosaic border cell clusters containing *crb*^{j1B5} mutant clones, the detailed migration delay analysis is in (F). (C) An egg chamber contains a Flip-out follicle cell clone that expressed *patj RNAi*. Antibody staining revealed that Patj level was strongly reduced in the clone. (G) Mosaic border cell clusters containing *patj* or *sdt* mutant clones resulted in ectopic actin patches. Dashed lines outline the *patj* or *sdt* mutant clone. Scale bars: 10μm.

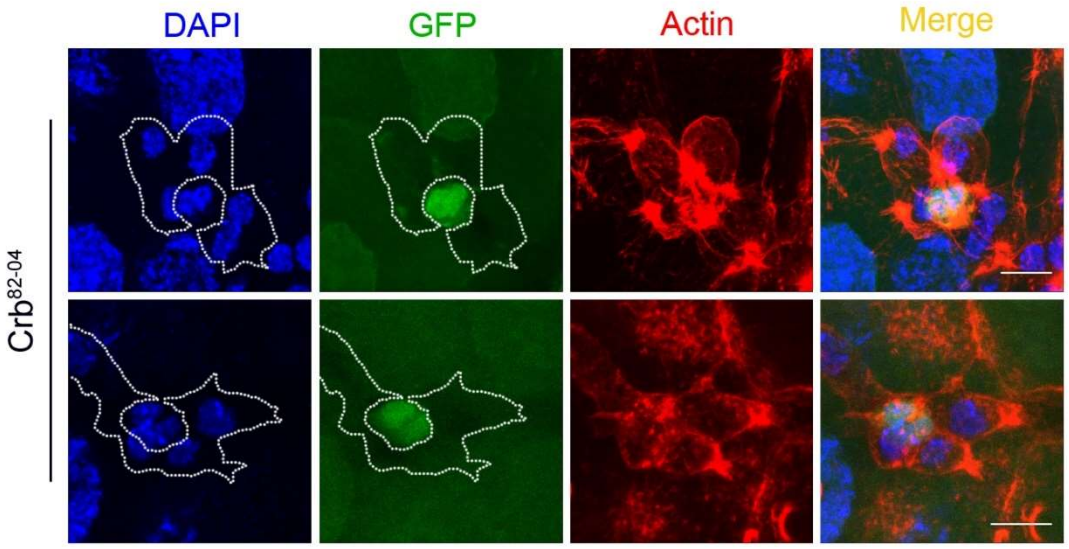

Figure S2. The *crb*$^{82\text{-}04}$ phenotype of ectopic actin patches is autonomous to border cells. The top row and bottom row each shows a mosaic cluster containing two central polar cells that are wild type or heterozygous (GFP positive, their DAPI-labeled nuclei smaller than those of adjacent border cells). The rest of the mosaic cluster is composed of a clone of *crb*$^{82\text{-}04}$ mutant outer border cells, which are indicated by lack of GFP and outlined by a dashed line. Wild type polar cells do not prevent the entire cluster from exhibiting the ectopic actin patches phenotype. The *crb*$^{82\text{-}04}$ mosaic cluster shown in the top row is the same cluster shown in Fig. 1C, except that the images here are derived from maximum projection of a z-series of confocal sections but the image in Fig. 1C is

a single confocal section. The bottom mosaic cluster is also shown in Fig. 4G, and the images are all resulted from maximum projection of a z-series of confocal sections. Scale bars: 10μm.

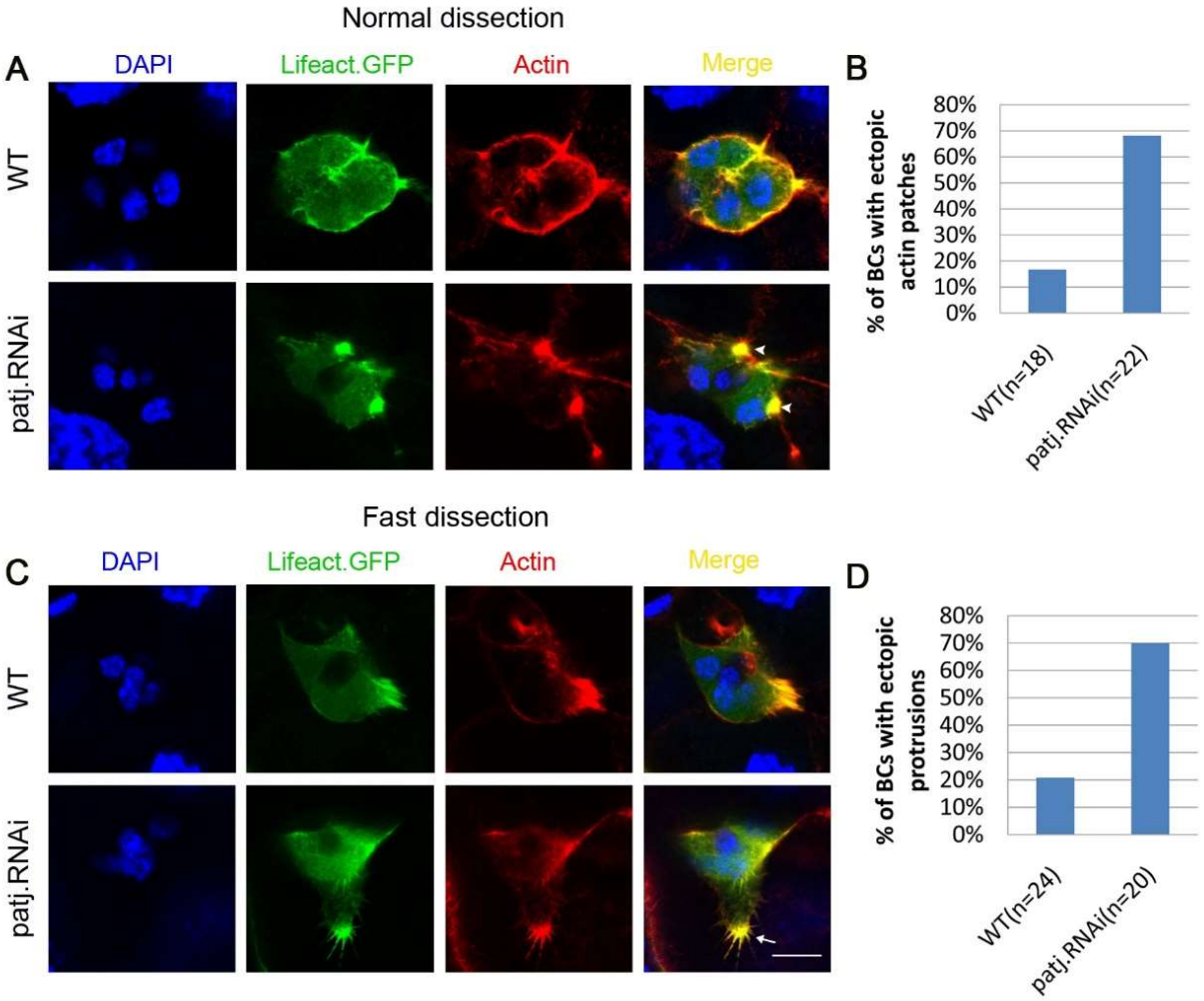

Figure S3. Fast dissection reveals fine structures of ectopic actin patches.

(A, B) After normal dissection and immunostaining (ovaries were dissected in cold PBS and the process would last about 20 minutes or above), typical wild type (WT) border cells extended a leading protrusion at the front, but *patj RNAi* border cells exhibited large ectopic actin patches at the side of cluster. Arrowheads indicate actin patches. Quantification for actin patches indicates that 68% of *patj RNAi* expressing border cell clusters (n=22) displayed ectopic actin patches. (C, D) After fast dissection and staining

(ovaries were dissected in cold PBS but the whole process was limited to less than 5 minutes), both the predominant protrusion at the leading edge in WT border cells and the ectopic actin patch in *patj RNAi* border cells exhibited finer details, which are characteristics of lamellipodial protrusion. Arrow indicates ectopic protrusion. Quantification indicates that 70% of patj RNAi clusters (n=20) displayed ectopic protrusions with fast method. The above results nicely confirmed that the actin patches observed using normal method are actually ectopic protrusions that displayed dynamic actin structures. F-actin is labeled by both Lifeact-GFP (green) and phalloidin-TRITC (red). Scale bar: 10μm.

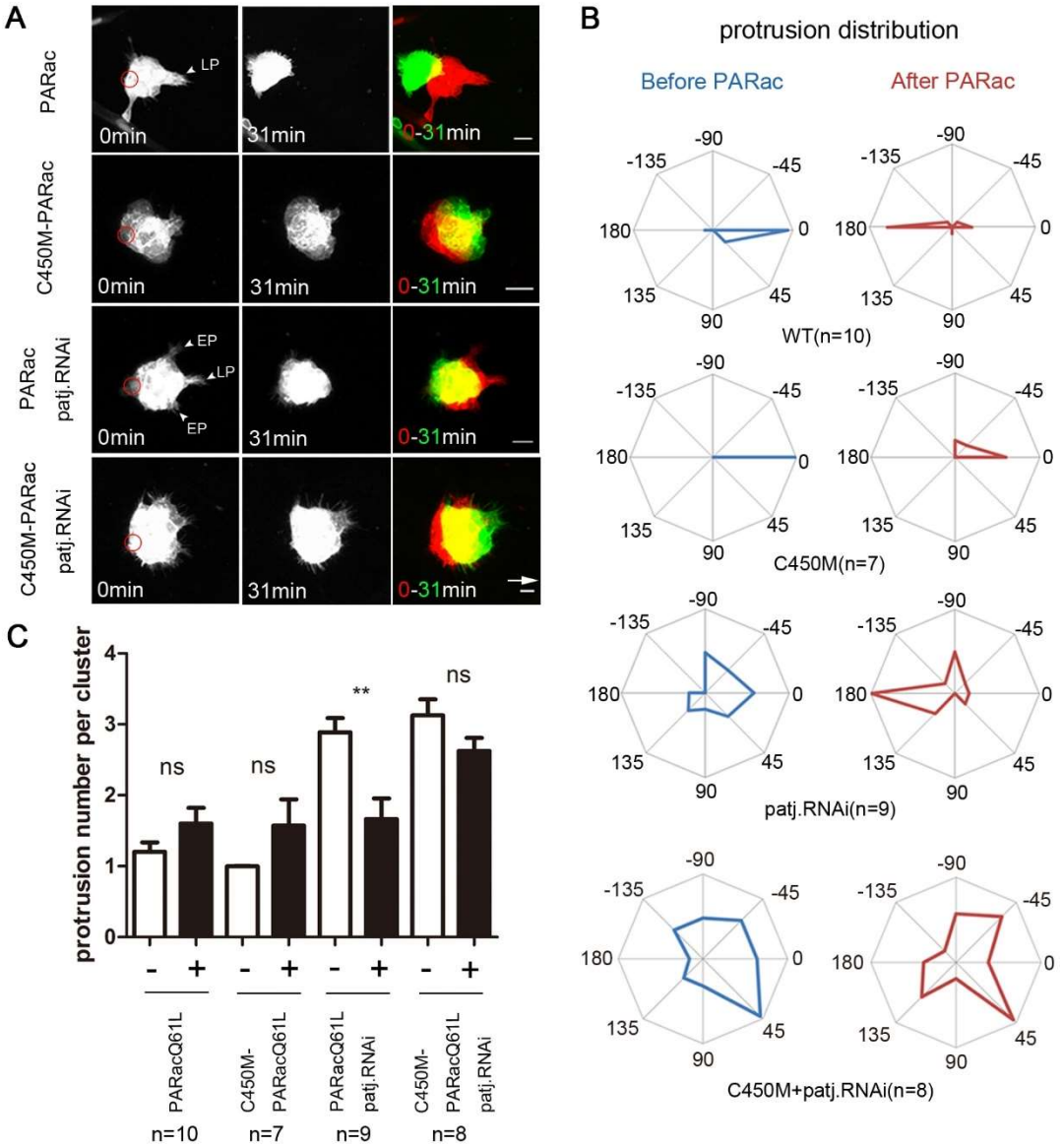

Figure S4. Loss of Patj does not affect non-autonomous cell-cell communication.

(A) Confocal images in the top panels (WT control) show that local photoactivation of PA-Rac by laser (red circle) in the back border cell induced a new protrusion, caused retraction of the leading protrusion, and redirected the whole cluster to move in an opposite direction, demonstrating effective cell-cell communication between the back cell and leading cell. The second row panels show that photoactivation of the photo-insensitive C450M-PA-Rac failed to achieve the above results, serving as a negative control (Wang et al., 2010). The third row panels show that local photoactivation of PA-Rac in the back cell of *patj RNAi* cluster not only retracted the leading protrusion but also retracted two ectopic protrusions on the side. Redirection of collective movement of cluster was also achieved. On the contrary, the bottom panels show that photoactivation of C450M-PA-Rac in *patj RNAi* background failed to result in retraction of ectopic protrusions and redirection of migration. White arrow indicates border cells' normal migration direction, which is to the right for all figures. White arrowheads point to leading protrusion (LP) and ectopic protrusion (EP). (B) Analysis of protrusion distribution by radar diagram, which divides the border cell cluster into 8 sectors. In the WT control, most of protrusions were aligned toward 0º (front) before PA-Rac photoactivation, but were switched toward 180º (back) after photoactivation. Such a switch in protrusion distribution is evident in *patj RNAi* but not in the C450M negative controls. (C) Quantification of average protrusion number per cluster reveals that a strong and significant reduction of protrusion number between before photoactivation (-) and after photoactivation (+) was only observed for *patj RNAi*. **, $P < 0.01$; ns, not significant; unpaired t-test; error bars indicate s.e.m. Scale bars: 10 µm.

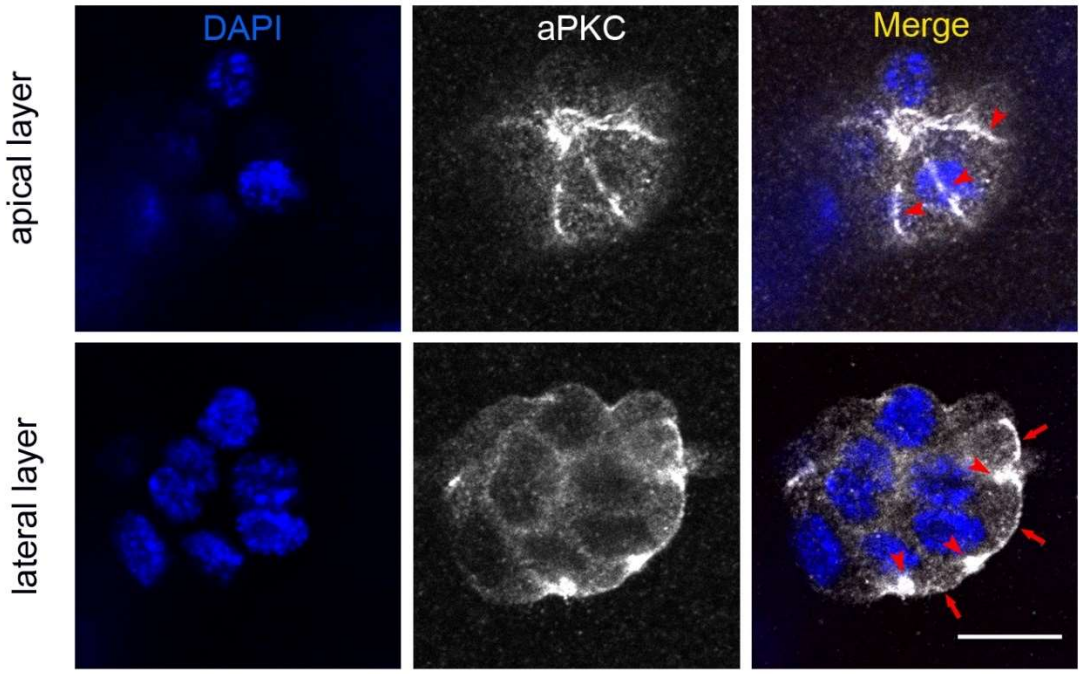

Figure S5. The two distinct pools of aPKC are best captured at two different focal planes within the same border cell cluster. The top row shows the single section confocal images of a border cell cluster at the apical layer/plane. Long lines of strong aPKC staining (indicated by red arrowheads) represent the major pool of membrane-bound aPKC at apical junctions between adjacent border cells. At this focal plane, the second minor pool of aPKC that is localized close to the outside lateral membrane is not obvious. Moving more basally to the lateral focal plane, the second pool of aPKC comes into view as thin lines or dots of moderate staining near the outside lateral membrane (indicated by red arrows) in the bottom row of confocal images. Meanwhile, the apical junctional staining of aPKC are mostly out of focus except for the remaining large spots (indicated by the red arrowheads), which are the most distal part of apical junctions between adjacent border cells. Note that between the large spots of junctional aPKC staining lies the second pool of aPKC (indicated by red arrows). Scale bars: 10 μm.

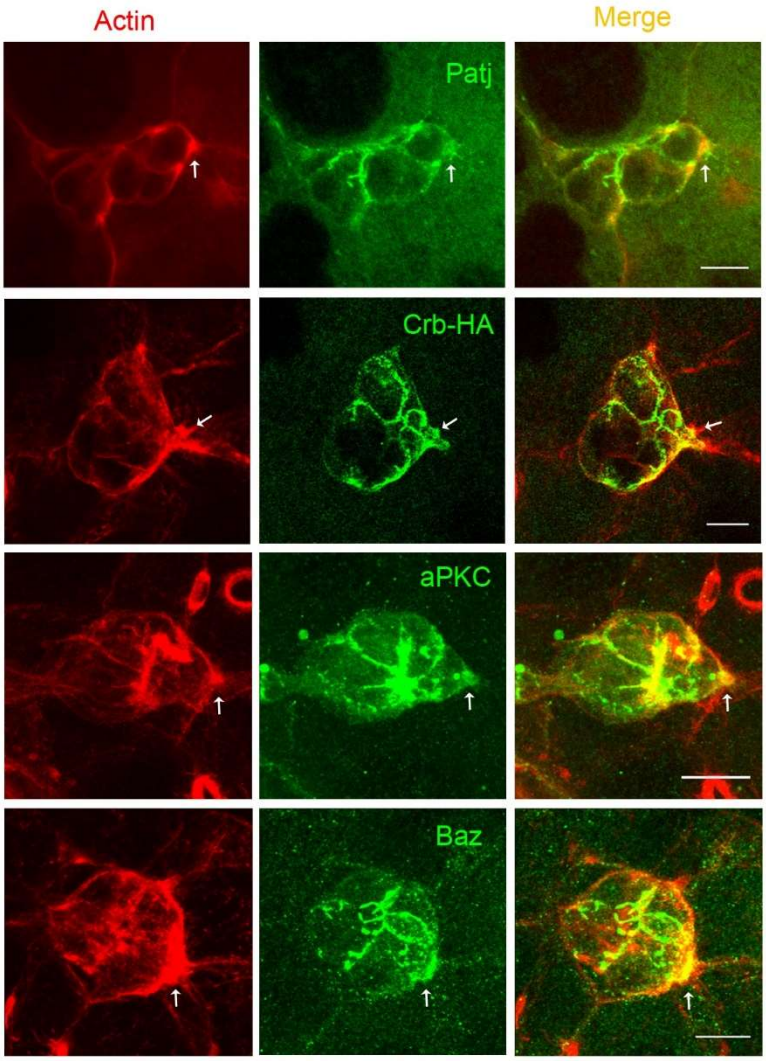

Figure S6. The second pool of apical polarity proteins is often observed to be enriched in leading protrusions. Patj, Crb-HA, aPKC and Baz are shown to be enriched (indicated by white arrows) in the leading protrusions of wild type border cell clusters. Because the apical junctional pool and the second pool near outside lateral membrane cannot be easily captured in one confocal image, we have to generate maximum projections of z-series to show both pools for Crb-HA, aPKC and Baz. The top row of Patj images is from single confocal sections, the same cluster is also shown in Fig. 3A (Patj). F-actin was labeled by phalloidin (red). Scale bars: 10 μm.

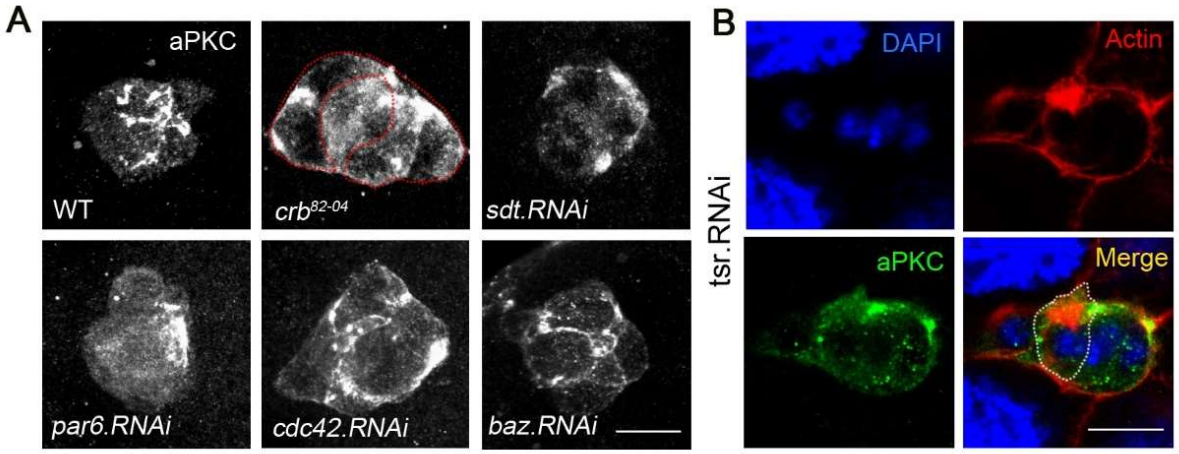

Figure S7. Distribution of aPKC caused by loss of function of Crb, Sdt, Par6, Cdc42, Baz and cofilin.

(A) Confocal images showing that loss of Crb complex components (Crb and Sdt) or Par complex components (Par6, Cdc42 but not Baz) severely disrupted the distribution of aPKC in the apical junctions. Reduction of Baz did not grossly affect the aPKC's distribution pattern. Dotted red line outlines the mutant *crb*$^{82\text{-}04}$ clone in the cluster. (B) One border cell cluster containing a single cell flip-out clone expressing *tsr RNAi* (*tsr* encodes cofilin) resulted in a large ectopic actin patch inside the clone, but no aPKC staining was colocalized with the actin patch. Scale bars: 10μm.

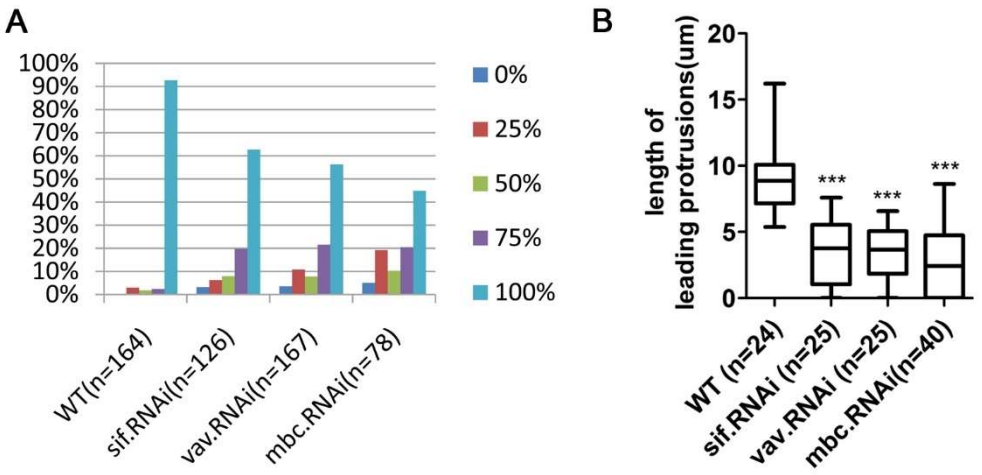

Figure S8. Knockdown of *sif*, *vav or mbc* resulted in migration defects and shortening of leading protrusions.

(A) *sif*, *vav,* or *mbc RNAi* each caused migration delay and (B) significant reduction of leading protrusion length, which is quantified and represented by the box and whisker plots. The box ranges from the 25th to the 75th percentiles, the whiskers represent the minimum and maximum values, and the line indicates the median value. *** $P < 0.001$; unpaired t-test.

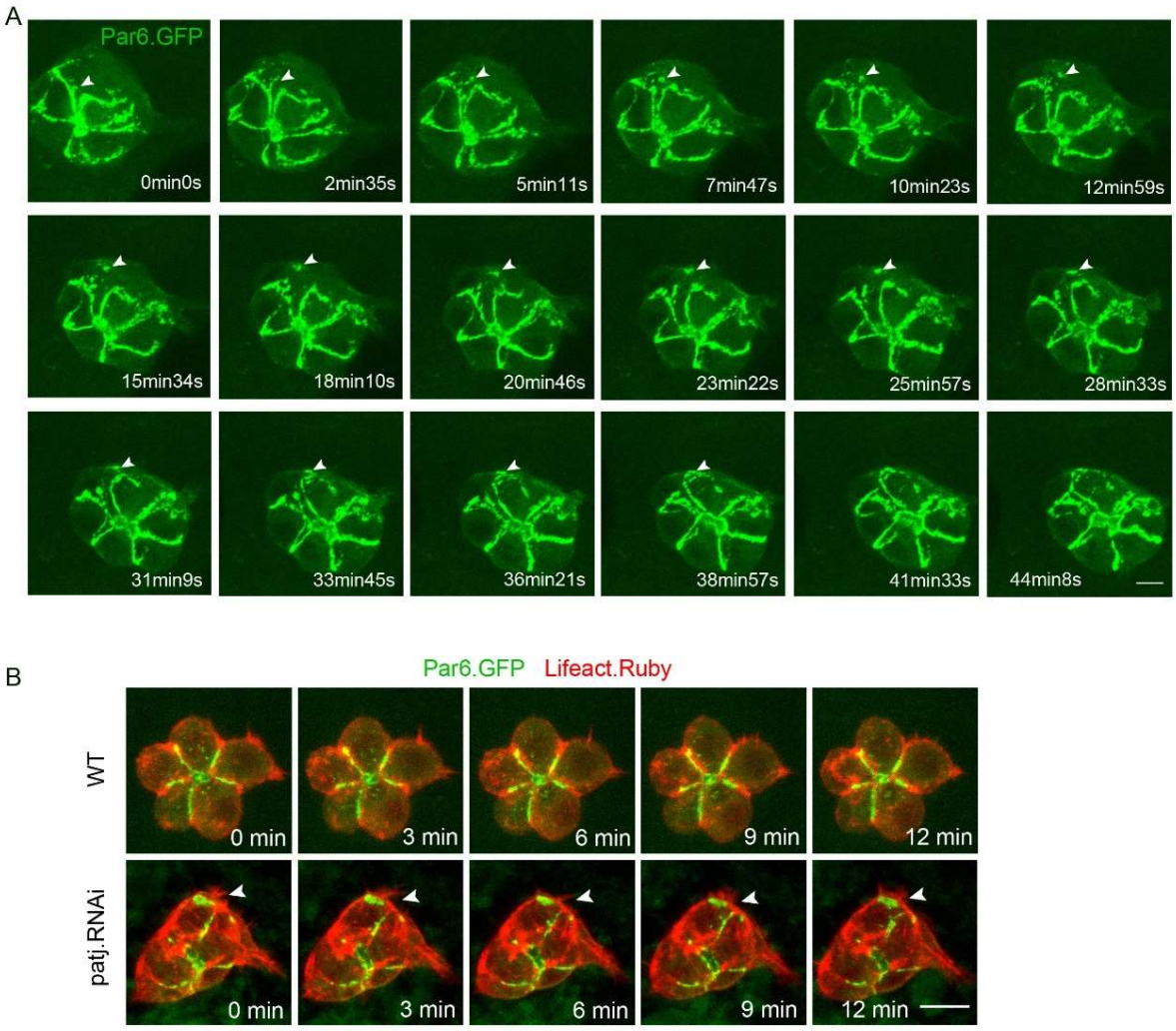

Figure S9. Dynamic distribution of Par6-GFP in WT and *patj RNAi* border cells.

(A) Time lapse images showing the dynamic distribution pattern of Par6-GFP in WT border cells. Par6-GFP signals mainly accumulated as lines at the apical junctions but they could be observed detaching from junctions as dots and moving toward the outer cortex. Arrowhead points to such a dot. (B) Time lapse images showing ectopic actin-rich protrusions extended from the position where an ectopic Par6-GFP patch was present as a result of loss of Patj (the second row), but this phenomenon could not be found in WT control (the first row). F-actin was labeled by Lifeact-Ruby (red). Arrowhead highlights the ectopic protrusion. Scale bar: 10μm.

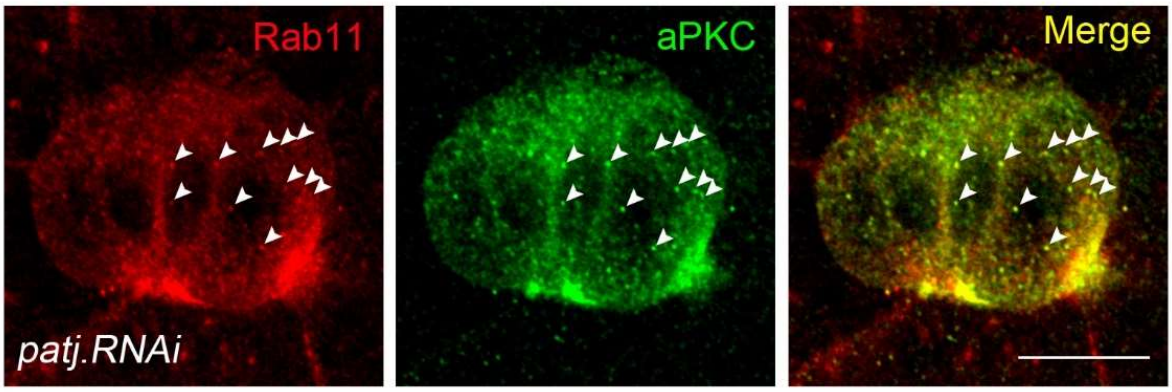

Figure S10. A high level of recycling is associated with large ectopic aPKC spots. In *patj RNAi* border cells, locally enriched recycling vesicles/endosomes were shown to partially localize with large ectopic aPKC patches near the outside membrane. In addition, Rab11-labeled recycling vesicles were shown to clearly colocalize with small aPKC dots in the cytoplasm (colocalizations indicated by white arrowheads). The images were captured using the latest Zeiss 880 Airyscan technology for high resolution imaging (achieving a maximum resolution of 120 nm in the x-y plane according to the manufacturer, which is close to super resolution quality). Scale bar: 10µm.

Table S1. *UAS* stocks obtained from public *Drosophila* stock centers

Genotype	Stock #	Use frequency	Source
UAS-patj.RNAi	THU1704	++	Tsinghua University RNAi Stock Center (TURSC)
UAS-patj.RNAi	12021R-3	+	National Institute of Genetics (NIG)
UAS-patj.RNAi	31620	+	Vienna Drosophila Research Center (VDRC)
UAS-patj.RNAi	101877	+	VDRC
UAS-sdt.RNAi	THU1336	++	TURSC
UAS-sdt.RNAi	29844	+	VDRC
UAS-sdt.RNAi	15342R-2	+	NIG
UAS-aPKC.RNAi	THU5841	++	TURSC
UAS-aPKC.RNAi	105624	++	VDRC
UAS-baz.RNAi	5055R-1	++	NIG
UAS-baz.RNAi	5055R-2	++	NIG
UAS-baz.RNAi	2915	+	VDRC
UAS-baz.RNAi	2914	++	VDRC
UAS-par6.RNAi	19731	+	VDRC
UAS-par6.RNAi	THU3865	++	TURSC
UAS-sif.RNAi	5406R-2	++	NIG
UAS-sif.RNAi	5406R-3	++	NIG
UAS-sif.RNAi	25789	+	Bloomington Drosophila Stock Center (BDSC)
UAS-vav.RNAi	6241	++	VDRC
UAS-mbc.RNAi	TH02182.N	+	TURSC
UAS-mbc.RNAi	TH02150.N	++	TURSC
UAS-mbc.RNAi	THU0808	++	TURSC
UAS-mbc.RNAi	TH01095.N2	+	TURSC
UAS-cdc42.RNAi	12530R-2	++	NIG
UAS-cdc42.RNAi	12530R-3	++	NIG
UAS-cdc42.RNAi	29004	+	BDSC
UAS-crb	5544		BDSC
UAS-Rab5-DN	9771		BDSC
UAS-Rab11-DN	23261		BDSC
UAS-Shi-DN	108437		KYOTO Stock Center (DGRC)
UAS-Shi-DN	108445		DGRC
UAS-clc.GFP	7107		BDSC
UAS-sif	9127		BDSC
FRT82B crb[j1B5]/TM6B	111051		DGRC
UAS-GFP	1522		BDSC
UAS-RacN17	6292		BDSC
UAS-patj	39735		BDSC
UAS-tsr.RNAi	110599		VDRC
UAS-Lifeact.Ruby	35545		BDSC
UAS-Lifeact.GFP	35544		BDSC

++ RNAi stocks more frequently used in this study.

+ RNAi stocks sometimes used in this study.

Movies

Movie 1. Live imaging of collective migration of a wild type (WT) border cell cluster. The border cells are shown migrating as a coherent cluster, with a large, predominant protrusion at the leading position. UAS-lifeact-GFP was expressed to label F-actin enriched structures such as protrusions in this and all subsequent movies. See Materials and Methods for details on live imaging. Scale bar: 10µm.

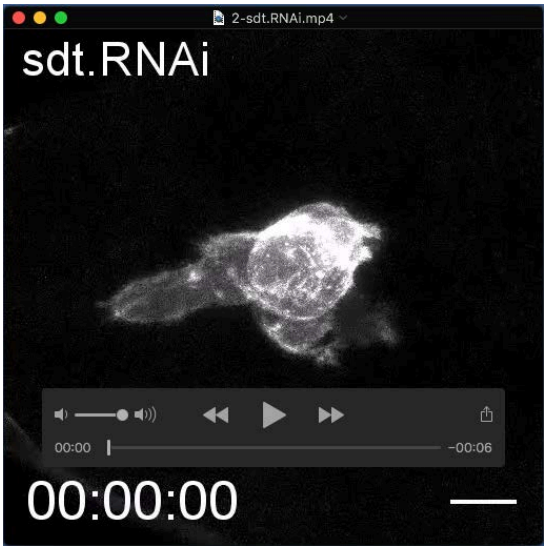

Movie 2. Live imaging of migrating border cells that are expressing *sdt RNAi.* The border cell cluster is shown extending several large ectopic protrusions during migration. The genotype of border cells is *slbo-Gal4, UAS-sdt RNAi, UAS-Lifeact-GFP*. All the transgenes and *RNAi* constructs were expressed using *slbo-Gal4,* a border cell-specific *Gal4* driver in this and subsequent movies. Scale bar: 10µm.

Movie 3. Live imaging of collective migration of *patj RNAi* expressing border cells. The *patj RNAi* border cells extend several ectopic protrusions in random directions during migration. Scale bar: 10µm.

Movie 4. Additional expression of *aPKC-DN* or *sif RNAi* rescues the ectopic protrusions phenotype exhibited by *patj RNAi* expression. Reducing the function of aPKC (by *aPKC-DN* expression), or Sif (by *sif RNAi* expression), in the background of *patj RNAi* expression, rescued the phenotype of ectopic protrusions. Note that the leading protrusions are also significantly shortened. Scale bars: 10µm.

Movie 5. Live imaging of border cell clusters expressing different mutant forms of aPKC. Expressing the dominant negative form of aPKC (aPKC-DN) resulted in suppression of leading protrusion formation, even though dynamic filopodial structures were seen forming randomly. In contrast, expression of the overactivated forms of aPKC (aPKC-CAAX and aPKC-CA) resulted in formation of large ectopic protrusions. Their clusters are much less coherent than the wild type clusters, individual border cells appear stretched outward. Scale bars: 10µm.

Movie 6. Sif overexpression resembles the aPKC-CAAX phenotype while *sif RNAi* rescues aPKC-CAAX's phenotype. Sif overexpression resembles the aPKC-CAAX phenotype that displays large ectopic protrusions and outstretched border cells. Expression of *sif RNAi* rescues aPKC-CAAX's phenotype. Scale bars: 10µm.

Movie 7. Expression of aPKC-DN fails to rescue the ectopic protrusions phenotype of Sif overexpression. Co-expression of the dominant negative form of aPKC (aPKC-DN) with Sif resulted in the same phenotype of expressing Sif alone. Scale bars: 10µm.